

Nitrogen-doped carbon quantum dots decorated on platinum catalysts for improved oxygen reduction reaction

Hyun-Gi Jo, Kue-Ho Kim, Hyo-Jin Ahn*

Department of Materials Science and Engineering, Seoul National University of Science and Technology, Seoul 01811, South Korea

ARTICLE INFO

Keywords:

Platinum nanoparticles
N-CQDs
Catalysts
Oxygen reduction reaction
Long-term stability

ABSTRACT

Nitrogen-doped carbon quantum dots (N-CQDs) decorated on platinum (Pt) nanoparticles (Pt@N-CQDs) were synthesized for use as catalysts in the oxygen reduction reaction (ORR). Pt@N-CQDs were prepared by hydrothermal and reduction methods, and an optimum concentration of N-CQDs was demonstrated. The weight percentage of CQDs to Pt was tested at 10, 20, and 30 wt% to optimize the ORR performance. In particular, Pt@20N-CQDs with 20 wt% N-CQDs exhibit superior electrochemical performance, such as onset potential (E_{onset}) of ~ 0.925 V, half-wave potential ($E_{1/2}$) of ~ 0.834 V, and limited-current density of -3.83 mA cm $^{-2}$ at 0.5 V. In the durability test for ORR catalytic activity, Pt@20N-CQDs showed low potential degradation and superior long-term stability of 20 mV (90.6%) at $E_{1/2}$ after 5000 cycles in 0.1 M KOH electrolyte. These performance improvements are owing to improved electrical properties by N doping in the CQDs and the increased number of active sites with oxygen-containing functional groups.

1. Introduction

Together with the development of next-generation sustainable energy conversion devices, the oxygen reduction reaction (ORR) has attracted considerable attention. The ORR is a key electrochemical process for eco-friendly energy conversion and storage devices [1–5]. In particular, the ORR at the cathode, which is more difficult and slower than the anodic reaction, is an important factor in determining the performance of devices [6,7]. Although Pt-based catalysts have been the best to date for the ORR process, they possess high overpotentials in both acidic and alkaline electrolytes and low long-term stability [8–11]. Despite extensive study, catalyst design is proceeding slowly due to the complex reaction mechanism for the ORR. Therefore, most research has focused on rational synthetic methods for various Pt-based nanomaterials [12–14]. Recently, ORR catalysts have been dispersed on carbon-based supports with high electrical conductivity and specific surface area such as carbon black, graphene, graphene oxide, and carbon nanotubes [15–21]. However, commercial carbon support materials, including carbon black (Vulcan XC-72), have unsatisfactory disadvantages such as low catalytic activity and durability [22]. To overcome these problems, carbon quantum dots (CQDs) are of considerable interest as ORR catalysts owing to their excellent electrical conductivity, oxygen-functional groups, and hydrophilicity [23–25]. Thus, studies on

N-CQDs decorated on Pt catalysts for optimum catalytic activity and improved long-term durability have yet to be reported.

In this paper, we propose a novel hybrid nanostructure combining N-CQDs and Pt catalysts using hydrothermal and reduction methods. We verified the optimized electrochemical properties this structure by demonstrating the relationships between morphology, structure, chemical bonding states, ORR activity, and long-term stability. In addition, N-doping was used to accelerate electrical conductivity on the CQDs for high-performance ORR activities.

2. Experimental details

Citric acid ($C_6H_8O_7$, 99.5%), urea (CH_4N_2O , 99.0%), chloroplatinic acid hydrate ($PtCl_4$, 99.9%), 2-propanol (99.5%), sodium borohydride ($NaBH_4$, 98%), Nafion® perfluorinated resin solution, and potassium hydroxide (KOH, 85%) reagents were purchased from Sigma-Aldrich. All chemicals were used as received without further purification. N-CQDs were synthesized using the hydrothermal method. Citric acid (2.73 g) and urea (1.24 g) were dissolved in deionized water (30 mL). The prepared solution was transferred into a Teflon-lined stainless-steel autoclave and heated at 180 °C for 6 h. After, the autoclave was cooled down to room temperature, the resulting CQDs were centrifuged at 10,000 rpm for 20 min to remove any sediment. The light brown

* Corresponding author.

E-mail address: hjahn@seoultech.ac.kr (H.-J. Ahn).

supernatant solution was dialyzed using a 6–8 kD molecular weight cut-off (MWCO) membrane for 12 h. The resulting solution was dried in an oven at 50 °C for 24 h to obtain black N-CQDs. These were dispersed in water at a weight ratio of 10, 20, and 30 to the platinum precursor, and 0.28 mM chloroplatinic acid hydrate was added to this solution. Subsequently, 0.1 M sodium borohydride solution was added to the mixture. Pt nanoparticles were isolated using freeze drying at –50 °C for 12 h in vacuum. This process yielded three types of electrocatalysts: Pt@10N-CQDs, Pt@20N-CQDs, and Pt@30N-CQDs, representing the 10, 20, and 30 wt ratios of N-CQDs to the platinum precursor.

The crystal structures and morphologies of all samples were characterized using X-ray diffraction (XRD) (Rigaku D/Max-2500 diffractometer) and transmission electron microscopy (TEM) (Tecnai G2, KBSI Gwangju Center). The chemical binding states were analyzed by X-ray photoelectron spectroscopy (XPS) (ESCALAB 250). Electrochemical measurements were carried out using a potentiostat/galvanostat (PGSTAT302N, FRA32M, Metrohm Autolab) with a rotating disk electrode (RDE). A three-electrode system is composed of a working electrode (glassy carbon), a reference electrode (Ag/AgCl) (sat. KCl), and a counter electrode (Pt wire). Each catalyst was prepared as ink with a mixture, containing 10 mg of respective catalysts dispersed in 250 μL of 1:1 v/v ratio of water/2-propanol containing 50 μL of 20 wt% Nafion solution followed by ultrasonication for an hour and dispersed for three days. In succession, 1.8 μL of homogeneous prepared electrocatalyst ink solution was dropped on the surface of glassy carbon electrode with an area of 0.0706 cm^2 and dried at 50 °C for 30 min in an oven. All electrodes were prepared with Pt loading amount of 0.80 $\text{mg}_{\text{Pt}} \text{cm}^{-2}$. The electrolyte was 0.1 M KOH, which was purged with O_2 and Ar gas for 1 h before starting the electrochemical measurement. Cyclic voltammetry (CV) was performed at a scan rate of 50 mV s^{-1} in the range from 0.1 to 1.2 V in the Ar and O_2 -saturated 0.1 M KOH electrolyte. Linear sweep voltammetry (LSV) measurements were performed at rotational speeds of 100, 400, 900, 1600, and 2500 rpm at a scan rate of 5 mV s^{-1} in the range from 1.2 to 0 V in an O_2 -saturated 0.1 M KOH electrolyte. To investigate long-term electrocatalytic stability, an accelerated durability

test (ADT) was performed at a scan rate of 100 mV s^{-1} in the range from 0.6 to 1.0 V for up to 5000 cycles. After the ADT test, the LSV was measured at 1600 rpm at a scan rate of 5 mV s^{-1} in the range from 1.2 to 0 V in an O_2 -saturated 0.1 M KOH electrolyte.

3. Results and discussion

Fig. 1(a) shows UV–Vis spectrum and illustration photographs of N-CQDs solution. The suspension of N-CQDs showed brown under a daylight (left) and bright blue fluorescence (right) under a 365 nm UV light. The UV–Vis spectrum exhibited two absorption peaks at 210 and 330 nm, which indicate that the absorption peaks of the N-CQDs were attributed to $\pi\text{-}\pi^*$ and $n\text{-}\pi^*$ transition of the aromatic sp^2 domains including C=C, C=N, and C=O bonds [26]. Fig. 1(b) shows a schematic illustration of the Pt@N-CQDs, which proposed as a new catalyst structure through the interaction of Pt NPs for ORR activity. Fig. S1 shows the schematic illustration of the synthesis method for N-CQDs and Pt@N-CQDs. Fig. 1(c) shows the XRD patterns of all samples. The spectrum of the N-CQDs exhibited a broad peak around 25°, corresponding to the (0 0 2) plane of graphite. However, no peak ascribed to the N-CQDs was identified for the XRD patterns of Pt@10N-CQDs, Pt@20N-CQDs, and Pt@30N-CQDs. This is due to low concentration of the N-CQDs with amorphous carbon related to low diffraction intensity, which is beyond the limits of XRD detection [27,28]. The main diffraction peaks of Pt@10N-CQDs, Pt@20N-CQDs, and Pt@30N-CQDs were observed at 39.9°, 46.3°, 67.8°, and 81.5° correspond to the (1 1 1), (2 0 0), (2 2 0), and (3 1 1) planes of the metallic Pt phases (JCPDS card No. 87-0646), respectively [29]. The particle size was calculated using the Scherrer equation [30]:

$$D = 0.9\lambda/(\beta\cos\theta)$$

where λ is the X-ray wavelength, β is the full width at half maximum (FWHM), and θ is the Bragg angle. Using the equation, the average sizes of all electrocatalyst were calculated by inputting the (1 1 1), (2 0 0), and

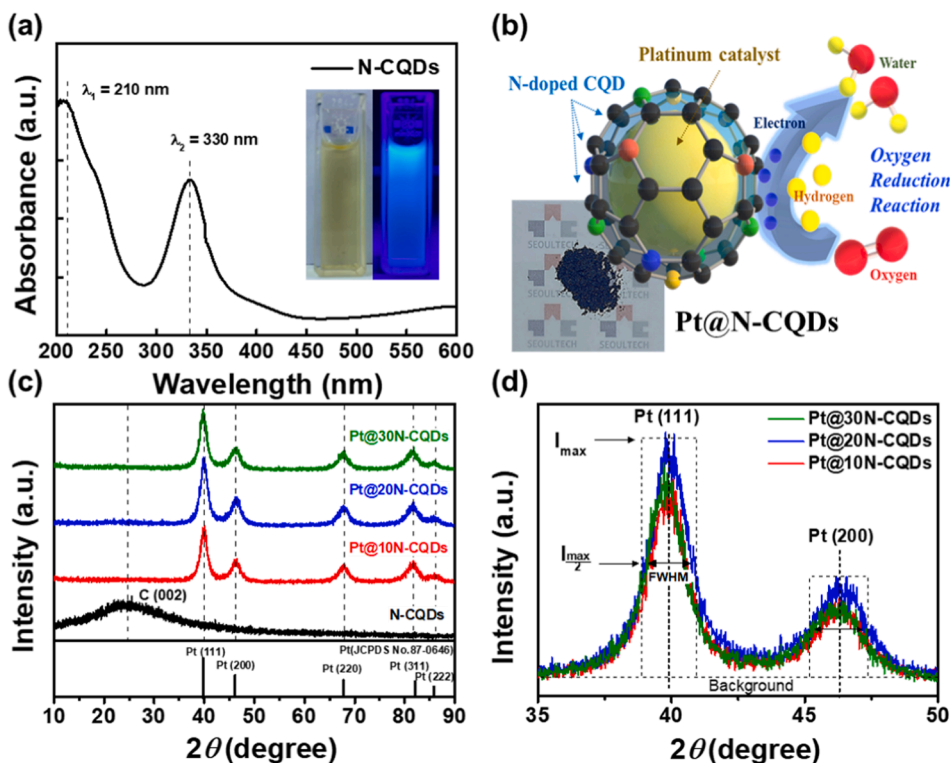


Fig. 1. (a) UV–Vis spectrum and illustration photographs of N-CQDs solution. (b) Schematic illustration of the Pt@N-CQDs (c) XRD patterns of N-CQDs, Pt@10N-CQDs, Pt@20N-CQDs, and Pt@30N-CQDs, and (d) FWHM data for the Pt(1 1 1) and Pt(2 0 0) peaks for Pt@10N-CQDs, Pt@20N-CQDs, and Pt@30N-CQDs.

(3 1 1) planes of the Pt phases (Fig. 1(d)). The average sizes of Pt@10N-CQDs, Pt@20N-CQDs, and Pt@30N-CQDs were ~ 4.48 , ~ 4.57 , and ~ 4.67 nm, respectively. Pt@20N-CQDs synthesized from the optimal concentration of N-CQDs can constitute the most ORR activity due to improved Pt crystallinity [31]. Crystal structure control and surface functional group formation of Pt-based catalysts are pivotal in improving stability [32]. However, excessive concentration of N-CQDs (for instance Pt@30N-CQDs) can lead to aggregation of N-CQDs and rather decrease the crystallinity of Pt [33]. As shown in Fig. S2, the FT-IR spectrum of N-CQDs observed these characteristic features in terms of the stretching vibrational peaks at 3446 cm^{-1} , 3214 cm^{-1} , 1662 cm^{-1} , 1631 cm^{-1} , 1577 cm^{-1} , 1394 cm^{-1} , and 1167 cm^{-1} , which were related to O-H, N-H/C-H, C=O, C=C, C-N, C-H, and N-H [34]. Compared to that of Pt NPs, the FT-IR spectrum of the Pt@20N-CQDs showed the peaks at 1577 cm^{-1} and 1167 cm^{-1} , which were caused by the stretching vibrations of C-N and N-H involvement of N-CQDs. These C-N and N-H groups confirm the formation of amide bonds due to the dehydration reaction between the amino and carboxyl groups [35]. Thus, FT-IR spectrum results signify that the nitrogen-doping and oxygen-containing functional groups of N-CQDs can effectively enhance the active sites of Pt NPs [36].

Fig. 2(a) shows a TEM image of N-CQDs with a size distribution range of 2–6 nm, which presents a relatively bright contrast. The HR-TEM image of the N-CQDs indicates a lattice fringe spacing of 0.34 nm, corresponding to the (0 0 2) plane of graphite (Fig. 2(b)) [37]. Fig. 2(c) shows the TEM image of Pt@20N-CQDs, which consist of relatively dark contrast Pt phases and relatively bright contrast N-CQDs. Their particle size distribution and average size are ~ 3 –5 nm and ~ 4.53 nm, which is slightly larger than the size of the Pt NPs. A lattice spacing of 0.227 nm, corresponding to the Pt (1 1 1) plane, was observed for the

HR-TEM image of Pt@20N-CQDs (Fig. 2(d)), [38,39]. The N-CQDs with lattice fringe spacings of 0.34 nm are distributed on the Pt nanoparticles [40]. As shown in the Fig. S3(a), Pt@10N-CQDs showed the lattice distance of 0.200 and 0.227 nm, corresponding to the (2 0 0) and (1 1 1) planes of the Pt FCC structure, respectively. Due to the low concentration of N-CQDs, the surface carbon layers of Pt@10N-CQDs are difficult to identify [41]. But, in Fig. S3(b), the Pt@20N-CQDs showed uniform carbon layers of ~ 1.7 nm on the surface of Pt NPs. In Fig. S3(c), uneven and aggregated carbon layers at the Pt@30N-CQDs were appeared due to the excessive concentration of N-CQDs. Thus, we confirmed that the structure of the Pt@N-CQDs can be adjusted by the concentration of N-CQDs and optimized at the Pt@20N-CQDs. Fig. S4(a) showed the TEM-EDS mapping data of the Pt@20N-CQDs, confirming uniformly distributed N-CQDs on the surface of Pt NPs [33]. In addition, well-distributed N and O elements with C elements indicate the successful formation of N-doped CQDs [42]. In Fig. S4(b) and (c), the map sum spectrum and EDS quantification results of Pt@20N-CQDs showed the quantified distribution of the Pt, C, N, and O elements [43]. As a result, it can be concluded that the Pt@20N-CQDs were composed of N-CQDs and Pt nanoparticles. Thermogravimetric analysis (TGA) curves of Pt@10N-CQDs, Pt@20N-CQDs, and Pt@30N-CQDs are shown in Fig. S5. The weight loss of Pt@N-CQDs begins at the room temperature and continues up to $540\text{ }^{\circ}\text{C}$, which is due to chemisorption of N-CQDs and loss of crystalline water [40,44]. Afterwards, the slower weight loss to $800\text{ }^{\circ}\text{C}$ may be due to the removal of oxygen-containing functionalities and volatile compounds such as CO, CO₂, H₂, and CH₄ in Pt@N-CQDs [45]. The Pt@10N-CQDs, Pt@20N-CQDs, and Pt@30N-CQDs showed the weight loss of 1.78, 4.12, and 8.89 wt%, respectively, which represents the N-CQDs amount of Pt@N-CQDs.

The chemical binding states of the N-CQDs and Pt@20N-CQDs were

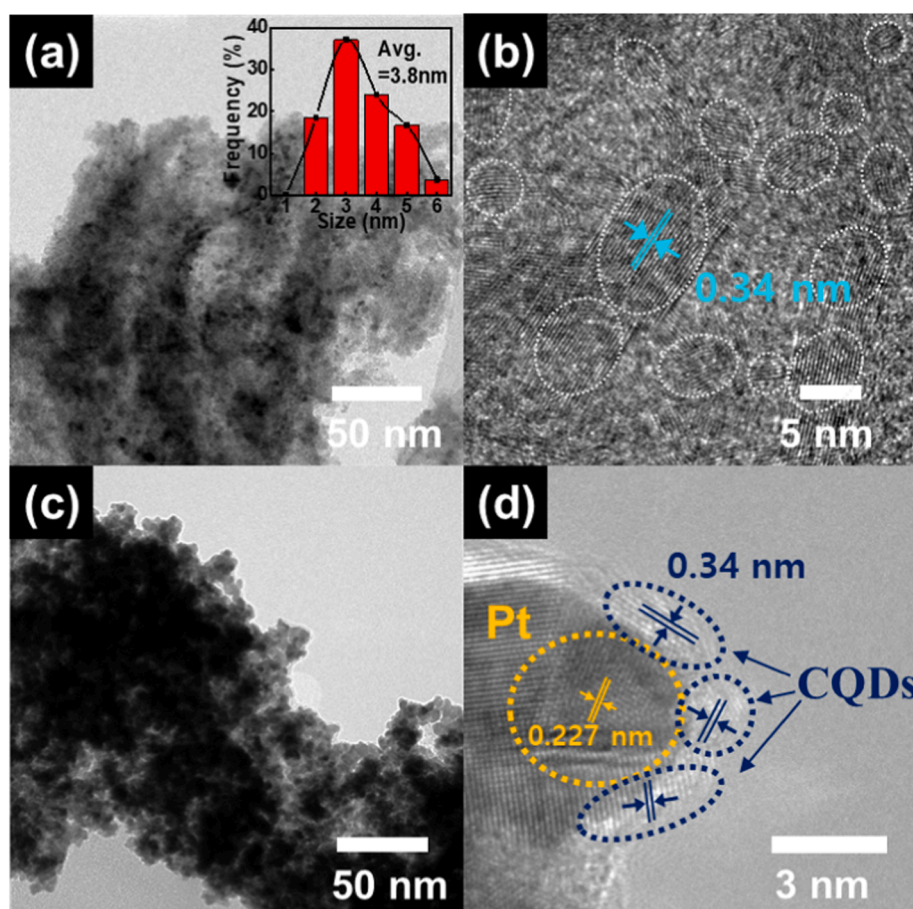


Fig. 2. (a) TEM and (b) HR-TEM images of N-CQDs, (c) TEM, and (d) HR-TEM images of Pt@20N-CQDs.

investigated by XPS measurements as shown in Fig. 3(a–f). Fig. 3(a) displays full-range XPS spectra of N-CQDs, Pt@20N-CQDs, and Pt NPs. In particular, Pt NPs show very low intensity of C without N elements. The XPS core-level spectra of C 1s and N 1s of Pt@20N-CQDs were generated due to N-CQDs, which is consistent with the chemical bonding state results of N-CQDs [46,47]. The C1s XPS core-level spectra of N-CQDs and Pt@20N-CQDs exhibited four peaks, including ~ 283.7 eV (C=C), ~ 284.7 eV (C–C), ~ 286.4 eV (C–N), and ~ 288.8 eV (O=C=O) (Fig. 3(b) and (e)) [36,39]. The oxygen-containing carbon atom as the carboxyl group has a relatively strong electro positivity, which is advantageous for adsorbing the oxygen atom of the oxygen and for further reduction of H_2O [48]. The N 1s XPS core-level spectra of N-CQDs and Pt@20N-CQDs showed three peaks including ~ 398.9 eV (pyridinic-N), ~ 400.3 eV (pyrrolic-N), and ~ 401.9 eV (graphitic-N) (see Fig. 3(c) and (f)). The pyridinic-N and pyrrolic-N are located on the edge of graphite, pyrrolic-N can contribute two p-electrons to the aromatic π -system, and pyridinic-N contributes only one p-electron [49,50]. These electron-rich N groups can activate the surrounding carbon atoms and generate a net positive charge, thereby promoting the ORR electrocatalytic activity of N-CQDs [51]. Fig. 3(d) shows the high-resolution Pt 4f spectra, which can be deconvoluted into two peaks: metallic Pt(0) at ~ 70.8 eV (Pt $4f_{7/2}$) and ~ 74.2 eV (Pt $4f_{5/2}$). The high proportion of Pt(0) phase in Pt@20N-CQDs can provide improved catalytic activity for oxygen adsorption.

Fig. 4(a) presents the electrocatalytic activity of Pt NPs, Pt@10N-CQDs, Pt@20N-CQDs, and Pt@30N-CQDs measured by CV. The electrochemical active surface area (ECSA) was calculated by integrating hydrogen adsorption charges of the CV curve. The ECSA value provides important information related to the number of catalytically active sites per mass (g) of the catalysts, and can be calculated using the following equation [52]:

$$ECSA(m^2 g^{-1}) = \frac{Q_H(\mu C cm^{-2})}{(21 \mu C cm^{-2}) \times m_{Pt}(g cm^{-2})}$$

where Q_H ($\mu C cm^{-2}$) is the measured coulombic charge for hydrogen desorption, $21 \mu C cm^{-2}$ is an assumed value for amount of adsorbed atomic hydrogen on clean Pt surface, and m_{Pt} ($g cm^{-2}$) is the amount of

Pt catalysts loading [53].

The specific ECSAs ($m^2 g^{-1}$) of all electrodes were 24.8, 34.6, 41.9, and $39.5 m^2 g^{-1}$ for Pt NPs, Pt@10N-CQDs, Pt@20N-CQDs, and Pt@30N-CQDs, respectively. Pt@20N-CQDs represent the largest ECSA, indicating more electrochemically available active sites compared with other samples [54]. This is because the optimized concentration of N-CQDs were well dispersed in the Pt NPs.

In order to more clearly identify the ORR activity, LSV measurements were performed as shown in Fig. 4(b). Pt@20N-CQDs showed an improved onset potential (E_{onset}) of ~ 0.925 V, half-wave potential ($E_{1/2}$) of ~ 0.834 V, and limited-current density of $-3.83 mA cm^{-2}$ at 0.5 V, which demonstrates enhanced ORR activity compared with the values (E_{onset} of ~ 0.871 V, $E_{1/2}$ of ~ 0.788 V, and limited-current density of $-2.91 mA cm^{-2}$) of the Pt NPs. The Pt@10N-CQDs and Pt@30N-CQDs samples also show higher E_{onset} and $E_{1/2}$ values than those of Pt NPs. These are summarized in Table S1.

The electrochemical reduction of O_2 proceeds in two main electron reaction pathways in alkaline electrolyte. One of the two pathways is the indirect transfer reaction of two-electrons ($2e^-$) to produce H_2O_2 and the other is the reaction of producing water (H_2O) through the direct four-electrons ($4e^-$) [55]. The difference between direct and indirect pathways is determined by the H_2O_2 molecules, participating to the reaction. Therefore, reducing H_2O_2 through four-electron paths is more favorable for ORR performance [56]. The selectivity of ORR was investigated according to the Koutecky-Levich (K-L) as the following equation [15]:

$$\frac{1}{j} = \frac{1}{j_k} + \frac{1}{j_d} = \frac{1}{B\omega^{1/2}} + \frac{1}{j_k}$$

where j is the measured current density, j_k and j_d are the kinetic-limited and diffusion-limited current density, k is electron transfer rate constant, ω is angular velocity of the electrode, and the proportionality coefficient (B) is calculated from the slope of the K-L plot based on the following equation:

$$B = 0.62nFC_0(D_0)^{2/3}v^{-1/6}$$

where n is the number of electrons transfer, F is the Faraday constant, C_0 is the bulk concentration of O_2 in the electrolyte, D_0 is the diffusion

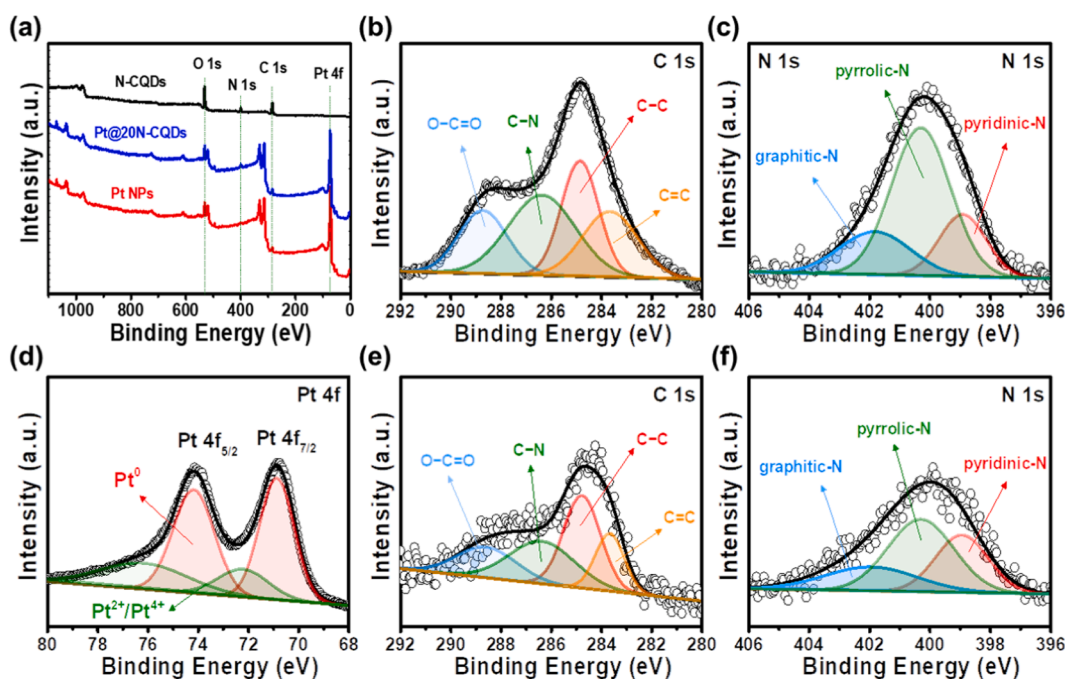


Fig. 3. (a) Wide-scan XPS spectra of N-CQDs, Pt@20N-CQDs, and Pt NPs and HR-XPS spectra of (b) and (e) C 1s, (c) and (f) N 1s, and (d) Pt 4f obtained from N-CQDs and Pt@20N-CQDs.

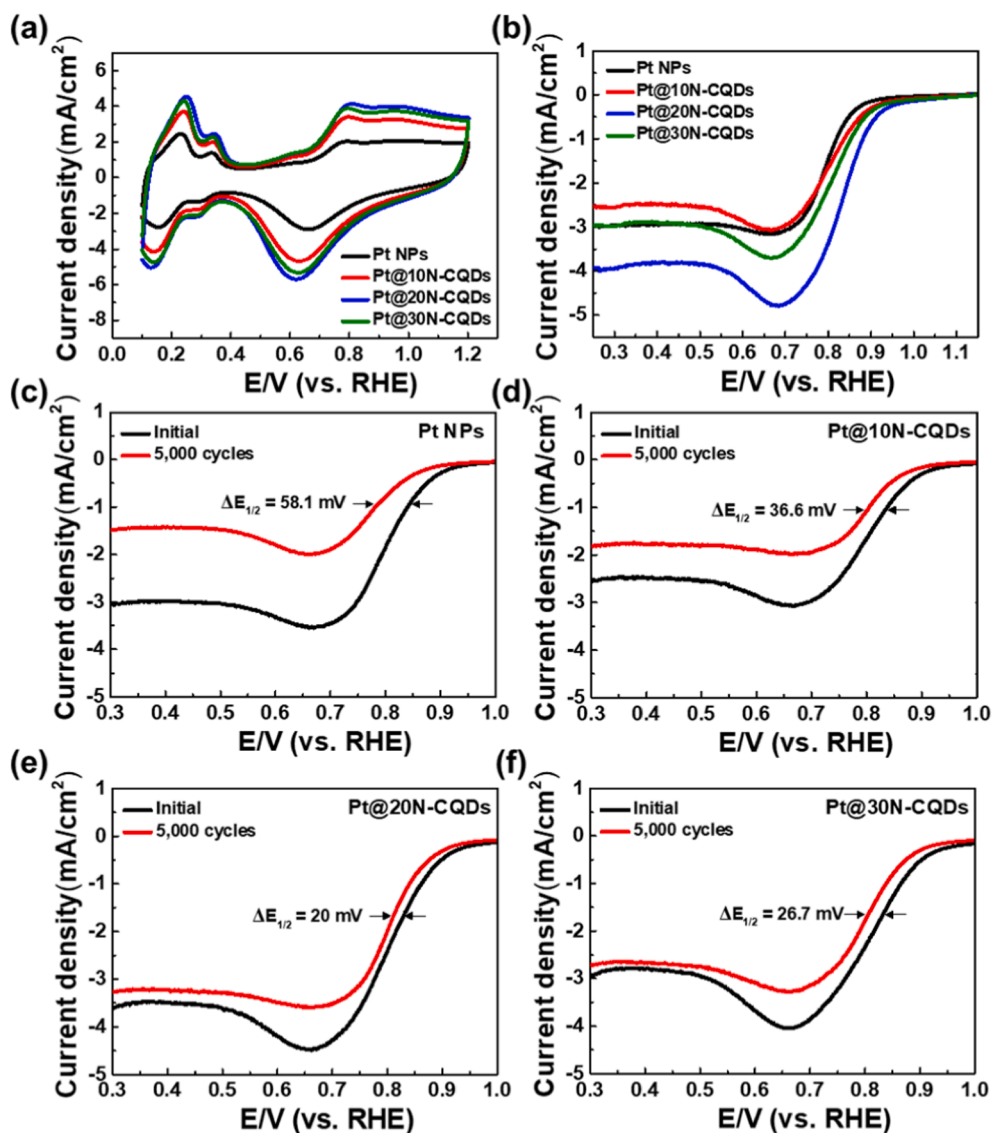


Fig. 4. (a) CV curves, (b) LSV curves of Pt NPs, Pt@10N-CQDs, Pt@20N-CQDs, and Pt@30N-CQDs, (c)–(f) initial and after accelerated durability test (ADT) of Pt NPs, Pt@N-10CQDs, Pt@20N-CQDs, and Pt@30N-CQDs.

coefficient of O_2 in the electrolyte, and ν is the kinematic viscosity of the electrolyte. Fig. S6(a) showed the LSV curves measured at 2500–400 rpm of Pt@20N-CQDs. It was calculated from the above equation and proving a four-electron reduction pathway with a K-L plot of 3.98 (≈ 4) in the range of 0.3–0.5 V (vs. RHE) (see Fig. S6(b)). Thus, Pt@20N-CQDs can induce an excellent ORR process in alkaline media due to the four-electron reduction pathway [42,45]. This performance improvement can be ascribed to two causes: one is due to N-doping of the CQDs, resulting in improved electronegativity on the carbon lattice, and the other is because of the increased number of active sites introduced by oxygen-containing functional groups on the CQDs. For practical applications as catalysts in fuel cells, the long-term stability test for ORR activity is one of the most important criteria. The ADT, which is more severe than the simple CV test due to rapid potential change and long-term cycling, was performed and the results are shown in Fig. 4(c–f). After 5000 cycles, the potential degradation of Pt NPs, Pt@10N-CQDs, Pt@20N-CQDs, Pt@30N-CQDs, evaluated at $E_{1/2}$ were 58.1, 36.6, 20.0, and 26.7 mV, respectively. Among all the samples, Pt@20N-CQDs showed superior long-term stability in ORR activity [57]. The well-decorated carbon layer obtained from an optimized N-CQD concentration plays a key role in protecting the catalytic degradation for improved

long-term stability [58]. On the other hand, Pt@30N-CQDs retain an excessive thick-decorated carbon layer from the excess concentration of N-CQDs, which yields a slightly reduced long-term stability compared to Pt@20N-CQDs. Therefore, we have demonstrated that well-decorated N-CQDs on Pt catalysts are a promising candidate as cathode catalysts for fuel cells.

4. Conclusion

In this work, N-CQDs decorated Pt catalysts were synthesized using hydrothermal and reduction methods. Pt@20N-CQDs showed improved ORR activity, including an E_{onset} of ~ 0.925 V, $E_{1/2}$ of ~ 0.834 V, and limited-current density of -3.83 mA cm^{-2} at 0.5 V. Furthermore, Pt@20N-CQDs showed excellent long-term stability, demonstrated by a low potential degradation of 20 mV (90.6%) in $E_{1/2}$ after 5000 cycles. The superior electrochemical performance is due to the improved electrical properties due to N doping of CQDs and the increased number of active sites provided by oxygen-containing functional groups on the N-CQDs. This demonstrates that Pt@N-CQDs are a promising technology for use as cathode catalysts in fuel cell applications.

CRedit authorship contribution statement

Hyun-Gi Jo: Conceptualization, Methodology, Investigation, Writing - original draft. **Kue-Ho Kim:** Methodology, Writing - original draft. **Hyo-Jin Ahn:** Conceptualization, Supervision, Writing - review & editing.

Declaration of Competing Interest

The authors declare that they have no known competing financial interests or personal relationships that could have appeared to influence the work reported in this paper.

Acknowledgements

This work was supported by the National Research Foundation of Korea (NRF) grant funded by the Korea government (MSIT) (No. 2019R1A2C1005836).

Appendix A. Supplementary material

Supplementary data to this article can be found online at <https://doi.org/10.1016/j.apsusc.2021.149594>.

References

- M. Li, Z. Zhao, T. Cheng, A. Fortunelli, C.-Y. Chen, R. Yu, Q. Zhang, L. Gu, B. V. Merinov, Z. Lin, E. Zhu, T. Yu, Q. Jia, J. Guo, L. Zhang, W.A. Goddard III, Y. Huang, X. Duan, Ultrafine jagged platinum nanowires enable ultrahigh mass activity for the oxygen reduction reaction, *Science* 354 (2016) 1414–1419.
- A. Gómez-Marín, J. Feliu, T. Edson, Reaction mechanism for oxygen reduction on platinum: existence of a fast initial chemical step and a soluble species different from H_2O_2 , *ACS Catal.* 8 (2018) 7931–7943.
- R. Su, C. Xie, S.I. Alhassan, S. Huang, R. Chen, S. Xiang, Z. Wang, L. Huang, Oxygen reduction reaction in the field of water environment for application of nanomaterials, *Nanomaterials* 10 (2020) 1719.
- J. Liu, M. Jiao, L. Lu, H.M. Barkholtz, Y. Li, Y. Wang, L. Jiang, Z. Wu, D.-J. Liu, L. Zhuang, C. Ma, J. Zeng, B. Zhang, D. Su, P. Song, W. Xing, W. Xu, Y. Wang, Z. Jiang, G. Sun, High performance platinum single atom electrocatalyst for oxygen reduction reaction, *Nat. Commun.* 8 (2017) 15938.
- G.-H. An, E.-H. Lee, H.-J. Ahn, Well-dispersed iron nanoparticles exposed within nitrogen-doped mesoporous carbon nanofibers by hydrogen-activation for oxygen-reduction reaction, *J. Alloy. Compd.* 682 (2016) 746–752.
- Y. Nie, L. Li, Z. Wei, Recent advancements in Pt and Pt-free catalysts for oxygen reduction reaction, *Chem. Soc. Rev.* 44 (2015) 2168–2201.
- M. Shao, A. Peles, K. Shoemaker, Electrocatalysis on platinum nanoparticles: particle size effect on oxygen reduction reaction activity, *Nano Lett.* 11 (2011) 3714–3719.
- A.M. Gómez-Marín, E.A. Ticianelli, A reviewed vision of the oxygen reduction reaction mechanism on Pt-based catalysts, *Curr. Opin. Electrochem.* 9 (2018) 129–136.
- M. Liu, Z. Zhao, X. Duan, Y. Huang, Nanoscale structure design for high-performance Pt-based ORR catalysts, *Adv. Mater.* 31 (2019) 1802234.
- B. Zhang, Y. Xue, H. Sun, A. Jiang, Z. Li, J. Hao, A green synthesis of “naked” Pt and PtPd catalysts for highly efficient methanol electrooxidation, *RSC Adv.* 6 (2016) 56083–56090.
- Y.-G. Lee, G.-H. An, H.-J. Ahn, Protein-based carbon and platinum nanocomposites as electrocatalysts for methanol oxidation activity, *J. Alloy. Compd.* 751 (2018) 62–68.
- K. Yamamoto, T. Imaoka, W.-J. Chun, O. Enoki, H. Katoh, M. Takenaga, A. Sonoi, Size-specific catalytic activity of platinum clusters enhances oxygen reduction reactions, *Nat. Chem.* 1 (2009) 397–402.
- H. Na, H. Choi, J.-W. Oh, Y.E. Kim, S.R. Choi, J.-Y. Park, Y.S. Cho, Graphitic carbon-based core-shell platinum electrocatalysts processed using nickel nanoparticle template for oxygen reduction reaction, *Appl. Surf. Sci.* 533 (2020) 147519.
- Z. Wang, X. Yao, Y. Kang, D. Xia, L. Gan, Development of structurally ordered platinum ternary intermetallic electrocatalysts for oxygen reduction reaction, *Catalysts* 9 (2019) 569.
- Y.-G. Lee, H.-J. Ahn, Tri(Fe/N/F)-doped mesoporous carbons as efficient electrocatalysts for the oxygen reduction reaction, *Appl. Surf. Sci.* 487 (2020) 389–397.
- X. Zhou, J. Qiao, L. Yang, J. Zhang, A review of graphene-based nanostructural materials for both catalyst supports and metal-free catalysts in PEM fuel cell oxygen reduction reactions, *Adv. Energy Mater.* 4 (2014) 1301523.
- G.-H. An, E.-H. Lee, H.-J. Ahn, Well-dispersed iron nanoparticles exposed within nitrogen-doped mesoporous carbon nanofibers by hydrogen-activation for oxygen reduction reaction, *J. Alloys Compd.* 682 (2016) 746–752.
- Z. Zhao, Q. Sha, K. Ma, Y. Lu, Liquid-to-gas transition derived cobalt-based nitrogen-doped carbon nanosheets with hierarchically porous for oxygen reduction reaction, *Appl. Surf. Sci.* 509 (2020), 145365.
- H.-G. Jo, H.-J. Ahn, Accelerating the oxygen reduction reaction and oxygen evolution reaction activities of N and P Co-doped porous activated carbon for Li-O₂ batteries, *Catalysts* 10 (2020) 1316.
- Y.-G. Lee, H.-J. Ahn, Tri(Fe/N/F)-doped Mesoporous Carbons as Efficient Electrocatalysts for the Oxygen Reduction Reaction, *Appl. Surf. Sci.* 487 (2019) 389–397.
- G.-H. An, Y.-G. Lee, H.-J. Ahn, Multi-active sites of iron carbide nanoparticles on nitrogen@cobalt-doped carbon for a highly efficient oxygen reduction reaction, *J. Alloy. Compd.* 746 (2018) 177–184.
- D. Pan, X. Li, A. Zhang, Platinum assisted by carbon quantum dots for methanol electro-oxidation, *Appl. Surf. Sci.* 427 (2018) 715–723.
- R. Wang, K.-Q. Lu, Z.-R. Tang, Y.-J. Xu, Recent progress in carbon quantum dots: synthesis, properties and applications in photocatalysis, *J. Mater. Chem. A* 5 (2017) 3717–3734.
- W.-J. Niu, R.-H. Zhu, Yan-Hua., H.-B. Zeng, S. Cosnier, X.-J. Zhang, D. Shan., One-pot synthesis of nitrogen-rich carbon dots decorated graphene oxide as metal-free electrocatalyst for oxygen reduction reaction, *Carbon* 109 (2016) 402–410.
- X. Liu, H. Jiang, J. Ye, C. Zhao, S. Gao, C. Wu, C. Li, J. Li, X. Wang, Nitrogen-doped carbon quantum dot stabilized magnetic iron oxide nanoprobe for fluorescence, magnetic resonance, and computed tomography triple-modal in vivo bioimaging, *Adv. Funct. Mater.* 26 (2016) 8694–8706.
- Z. Song, F. Quan, Y. Xu, M. Liu, L. Cui, J. Liu, Multifunctional N, S co-doped carbon quantum dots with pH- and thermo-dependent switchable fluorescent properties and highly selective detection of glutathione, *Carbon* 104 (2016) 169–178.
- H. Huang, H. Ouyang, T. Han, H. Wang, X. Zheng, Construction of carbon quantum dots/single crystal TiO₂ nanosheets with exposed 001 and 101 facets and their visible light driven catalytic activity, *RSC Adv.* 9 (2019) 3532–3541.
- S. Zhao, C. Li, L. Wang, N. Liu, S. Qiao, B. Liu, H. Huang, Y. Liu, Z. Kang, Carbon quantum dots modified MoS₂ with visible-light-induced high hydrogen evolution catalytic ability, *Carbon* 99 (2016) 599–606.
- S.A. Abbas, S.-H. Kim, H. Saleem, S.-H. Ahn, K.-D. Jung, Preparation of metal amalgam electrodes and their selective electrocatalytic CO₂ reduction for formate production, *Catalysts* 9 (2019) 367.
- H.-C. Wu, T.-C. Chen, N.-C. Lai, C.-M. Yang, J.-H. Wu, Y.-C. Chen, J.-F. Leed, C.-S. Chen, Synthesis of sub-nanosized Pt particles on mesoporous SBA-15 material and its application to the CO oxidation reaction, *Nanoscale* 7 (2015) 16848–16859.
- N. Jung, Y.-H. Chung, D.Y. Chung, K.-H. Choi, H.-Y. Park, J. Ryu, S.-Y. Lee, M. Kim, Y.-E. Sung, S.-J. Yoo, Chemical tuning of electrochemical properties of Pt-skin surfaces for highly active oxygen reduction reactions, *Phys. Chem. Chem. Phys.* 15 (2013) 17079–17083.
- M. Liu, Z. Zhao, X. Duan, Y. Huang, Nanoscale structure design for high-performance Pt-based ORR catalysts, *Adv. Mater.* 31 (2018) 1802234.
- T. Liu, S. Sun, L. Zhou, P. Li, Z. Su, G. Wei, Polyurethane-supported graphene oxide foam functionalized with carbon dots and TiO₂ particles for photocatalytic degradation of dyes, *Appl. Sci.* 9 (2019) 293.
- M. Amjad, M. Iqbal, A. Faisal, A.M. Junjua, I. Hussain, S.Z. Hussain, H.A. Ghranh, K.A. Khan, H.A. Janjua, Hydrothermal synthesis of carbon nanodots from bovine gelatin and PHM3 microalgae strain for anticancer and bioimaging applications, *Nanoscale Adv.* 1 (2019) 2924–2936.
- A. Mehta, P. Devi, A. Thakur, S. Basu, Enhanced photocatalytic water splitting by gold carbon dot core shell nanocatalyst under visible/sunlight, *New J. Chem.* 41 (2017) 4573–4581.
- A. Zhang, X. Li, Y. He, Platinum/nitrogen-doped carbon nanoparticles synthesized in nitrogen-doped carbon quantum dots aqueous solution for methanol electro-oxidation, *Electrochim. Acta* 213 (2016) 332–340.
- G. He, Y. Song, K. Liu, A. Walter, S. Chen, S. Chen, Oxygen reduction catalyzed by platinum nanoparticles supported on graphene quantum dots, *ACS Catal.* 3 (2013) 831–838.
- S. Sun, Y. Wang, L. Wang, T. Guo, X. Yuan, D. Zhang, Z. Xue, X. Zhou, X. Lu, Synthesis of Au@nitrogen-doped carbon quantum dots@Pt core-shell structure nanoparticles for enhanced methanol electrooxidation, *J. Alloys Compd.* 793 (2019) 635–645.
- W. Wang, Z. Wang, M. Yang, C.-J. Zhong, C.-J. Liu, Highly active and stable Pt (111) catalysts synthesized by peptide assisted roomtemperature electron reduction for oxygen reduction reaction, *Nano Energy* 25 (2016) 26–33.
- Y. Zhu, X. Ji, C. Pan, Q. Sun, W. Song, L. Fang, Q. Chena, C.E. Banks, A carbon quantum dot decorated RuO₂ network: outstanding supercapacitances under ultrafast charge and discharge, *Energy Environ. Sci.* 6 (2013) 3665–3675.
- L. Xu, L. Yang, X. Bai, X. Du, Y. Wang, P. Jin, Persulfate activation towards organic decomposition and Cr(VI) reduction achieved by a novel CQDs-TiO_{2-x}/rGO nanocomposite, *Chem. Eng. J.* 373 (2019) 238–250.
- G. Muthusankar, A. Sangili, S.-M. Chen, R. Karkuzhali, M. Sethupathi, G. Gopu, S. Karthick, R.K. Devi, N. Sengottuvelan, In situ assembly of sulfur-doped carbon quantum dots surrounded iron (III) oxide nanocomposite; a novel electrocatalyst for highly sensitive detection of antipsychotic drug olanzapine, *J. Mol. Liq.* 268 (2018) 471–480.
- M. Wang, Q. Fu, K. Zhang, Y. Wan, L. Wang, M. Gao, Z. Xia, D. Gao, A magnetic and carbon dot based molecularly imprinted composite for fluorometric detection of 2,4,6-trinitrophenol, *Microchim. Acta* 186 (2019) 86.
- F. Zheng, Z. Wang, J. Chen, S. Li, Synthesis of carbon quantum dot-surface modified P25 nanocomposites for photocatalytic degradation of p-nitrophenol and acid violet 43, *RSC Adv.* 4 (2014) 30605–30609.

- [45] N.C.T. Martins, J. Angelo, A.V. Girao, T. Trindade, L. Andrade, A. Mendes, N-doped carbon quantum dots/TiO₂ composite with improved photocatalytic activity, *Appl. Catal. B-Environ.* 193 (2016) 67–74.
- [46] A. Muthurasu, S.V. Sheen Mers, V. Ganesh, Nitrogen doped graphene quantum dots (N-GQDs)/Co₃O₄ composite material as an efficient bi-functional electrocatalyst for oxygen evolution and oxygen reduction reactions, *Int. J. Hydrog. Energy* 43 (2018) 4726–4737.
- [47] Z. Duan, G. Henkelman, Identification of active sites of pure and nitrogen-doped carbon materials for oxygen reduction reaction using constant-potential calculations, *J. Phys. Chem. C* 124 (2020) 12016–12023.
- [48] R.-S. Zhong, Y.-H. Qin, D.-F. Niu, J.-W. Tian, X.-S. Zhang, X.-G. Zhou, S.-G. Sun, W.-K. Yuan, Effect of carbon nanofiber surface functional groups on oxygen reduction in alkaline solution, *J. Power sources* 225 (2013) 192–199.
- [49] H. Lu, Y. Huang, J. Yan, W. Fan, T. Liu, Nitrogen-doped graphene/carbon nanotube/Co₃O₄ hybrids: one-step synthesis and superior electrocatalytic activity for the oxygen reduction reaction, *RSC Adv.* 5 (2015) 94615–94622.
- [50] D.-Y. Shin, K.-W. Sung, H.-J. Ahn, Synergistic effect of heteroatom-doped activated carbon for ultrafast charge storage, *Appl. Surf. Sci.* 478 (2019) 499–504.
- [51] J. Cao, Y. Hu, L. Chen, J. Xu, Z. Chen, Nitrogen-doped carbon quantum dot/graphene hybrid nanocomposite as an efficient catalyst support for the oxygen reduction reaction, *Int. J. Hydrog. Energy* 42 (2017) 2931–2942.
- [52] H. Zhu, X. Li, F. Wang, Synthesis and characterization of Cu@Pt/C core-shell structured catalysts for proton exchange membrane fuel cell, *Int. J. Hydrog. Energy* 36 (2011) 9151–9154.
- [53] A.L. Ong, K.K. Inglis, D.K. Wheligan, S. Murphy, J.R. Varcoe, Effect of cationic molecules on the oxygen reduction reaction on fuel cell grade Pt/C (20 wt%) catalyst in potassium hydroxide (aq, 1 mol dm⁻³), *Phys. Chem. Chem. Phys.* 17 (2015) 12135–12145.
- [54] G.-H. An, E.-H. Lee, H.-J. Ahn, Ruthenium and ruthenium oxide nanofiber supports for enhanced activity of platinum electrocatalysts in the methanol oxidation reaction, *Phys. Chem. Chem. Phys.* 18 (2016) 14859–14866.
- [55] R. Zhou, Y. Zheng, M. Jaroniec, S.-Z. Qiao, Determination of the electron transfer number for the oxygen reduction reaction: from theory to experiment, *ACS Catal.* 6 (2016) 4720–4728.
- [56] K. Kakaei, High efficiency platinum nanoparticles based on carbon quantum dot and its application for oxygen reduction reaction, *Int. J. Hydrog. Energy* 42 (2017) 11605–11613.
- [57] X. Tong, J. Zhang, G. Zhang, Q. Wei, R. Chenitz, J.P. Claverie, S. Sun, Ultrathin carbon-coated Pt/carbon nanotubes: a highly durable electrocatalyst for oxygen reduction, *Chem. Mater.* 29 (2017) 9579–9587.
- [58] C.H. Choi, H.C. Kwon, S. Yook, H. Shin, H. Kim, M. Choi, Hydrogen peroxide synthesis via enhanced two-electron oxygen reduction pathway on carbon-coated Pt surface, *J. Phys. Chem. C* 118 (2014) 30063–30070.